Wavefield simulation and reverse time migration for acoustic TTI media

Yi Zhang[*] [‡], **Alexey Stovas**[†] **and Luca De Siena**[*§]

[*] *Johannes Gutenberg University Mainz*

Saarstr. 21, 55122 Mainz, Germany

[†] *Norwegian University of Science and Technology*

Høgskoleringen 1, 7491 Trondheim, Norway

[‡] *Max Planck Graduate Center with the Johannes Gutenberg University of Mainz*

Forum universitatis 2, 55122 Mainz, Germany

[§] *Alma Mater Studiorum Bologna*

Viale Carlo Berti Pichat 8, 40127 Bologna, Italy

(January 23, 2024)

Running head: **Acoustic TTI wavefield and RTM**

Wavefield simulation and reverse time migration for acoustic TTI media

(January 23, 2024)

Running head: **Acoustic TTI wavefield and RTM**

ABSTRACT

Seismic imaging necessitates precisely separating P- and S-waves to mitigate undesirable crosstalk between them. Failure to properly handle this crosstalk can lead to distorted or misinterpreted images. In an elastic anisotropic medium, the polarization of a P-wave is not necessarily parallel to its propagating direction, making the separation of P- and S-waves harder than in the case of an elastic isotropic medium. A pure acoustic transversely isotropic (TI) wave equation involves a mixed-domain problem. This usually means the space dependencies and wavenumbers are coupled in the wavefield extrapolator. An efficient solution to the wavefield requires a separation between the space dependencies and wavenumbers in the extrapolator. There are two primary approaches: (1) An analytical separation of the mixed-domain term; (2) A numerical solution to the mixed-domain term, such as low-rank and Poynting vector methods. In this study, we derive the acoustic approximation by setting the S-wave phase velocity to zero in all directions. We propose an analytical separation by employing a Taylor series to linearize the anellipticity term, thereby decoupling the space-dependent and wavenumber-dependent variables within the wavefield extrapolator. The kinematics

analysis demonstrates that our method has competitive phase velocity accuracy compared to existing methods. Moreover, the corresponding TI acoustic wave equation can be efficiently solved by the hybrid finite-difference/pseudospectral method. In a 2D case, it only requires one fast Fourier transform, two inverse Fourier transforms and a few additional spatial differentiations at each time step. Remarkably, our wavefield solution remains independent of the wavefield heterogeneity (as observed in the low-rank approach) and is immune to wavefield interference (as encountered in the Poynting vector method). The proposed acoustic approximation ensures the absence of any S-wave artifacts with relatively cheap computation. Numerical examples show our proposed acoustic TTI wave equation is reliable for accurate wavefield modelling and reverse time migration (RTM).

INTRODUCTION

The acoustic wave equation is extensively utilized in geophysics for tasks such as modeling, migration, and inversion, primarily to mitigate issues related to crosstalk between P- and S-waves and parameter tradeoff (Li et al., 2015; Pestana et al., 2012; Yang and Zhu, 2018). Crosstalk refers to the situation in which the P- and S-wave components of both source and receiver wavefields are not entirely separated, resulting in interference between them. The challenge of parameter tradeoff arises because many inverse problems are ill-posed or underdetermined, demanding a delicate equilibrium between these parameters. Enhancing the estimation of one parameter often comes at the cost of the accuracy of others. The inverse problem for the elastic wave equation is inherently more intricate compared to the acoustic counterpart, making the elastic inverse problem more susceptible to issues related to parameter tradeoffs. The combination of crosstalk and parameter tradeoff can lead to the generation of artifacts, noise, and distortions in migrated images, particularly in anisotropic media, where wave propagation is direction-dependent (In the Christoffel equation, both the wave speed and the polarization are functions of the propagating direction). In addition, the acoustic wavefield is generally cheaper to solve than the elastic one. To obtain the acoustic wavefield, the separation of P- and S-waves in an elastic medium is necessary. Anisotropy is pervasive across Earth media and ignoring it can lead to severe distortions and loss of resolution in the final model (Thomsen, 2002). The polarization of a qP-wave (P-wave to remain concise) is not necessarily parallel to the propagating direction in an anisotropic medium. Thus, differently from an isotropic

medium, the anisotropic P-wavefield cannot be obtained by applying a Helmholtz decomposition to the elastic wavefield (Tsvankin, 2012).

The pure P-wave dispersion relation for anisotropic media introduces complexity as the space dependency and wavenumbers are coupled, making direct solutions of the resulting wave equation usually computationally expensive. Consequently, there are two general approaches to solving the pure acoustic wavefield efficiently: (1) Analytical methods involve formulating an acoustic wave equation with reduced complexity by separating space dependency and wavenumbers analytically (Alkhalifah, 1998a, 2000; Chu et al., 2011); (2) Alternatively, specialized numerical methods can be employed to separate space and wavenumbers. These methods include low-rank approximations (Song and Alkhalifah, 2013; Engquist and Ying, 2009; Cheng and Fomel, 2014) and the Poynting vector method (Xu and Zhou, 2014; Zhang and Ohen, 2022).

Under given approximations, the acoustic wave equation can be obtained analytically from the anisotropic elastic wave equation. For instance, by setting the vertical S-wave phase velocity to zero in the vertical transversely isotropic (VTI) elastic dispersion relation, Alkhalifah (1998a) and Alkhalifah (2000) obtained an acoustic VTI wave equation with fourth-order derivatives in both time and space. However, this form produces S-wave artifacts as the order of the characteristic equation from the Christoffel equation is 4, thus, it contains 2 wave modes corresponding to P-wave and S-wave artifacts. In practical applications, one always needs to taper the anellipticity (η) in the source region to suppress the S-wave artifacts. Following this, Zhou

et al. (2006) extend the work to tilt transversely isotropic (TTI) media, but it still contains S-wave artifacts and is not numerically stable with fast change of the tilt angle. To address the instability issue, Zhang et al. (2011) proposed a stable acoustic TTI equation, derived from Hooke's law and the equation of motion, but it still contains S-wave artifacts. Another approach to obtain the pure P-wave information is to expand the term of the square root in the P-wave dispersion using Taylor series (Chu et al., 2011), which is free from S-wave artifacts. However, to make a feasible numerical solution (separation between space dependencies and wavenumbers), one additional assumption has to be made: Horizontal P-wave phase velocity (v_{ph}) and vertical P-wave phase velocity (v_{pz}) satisfy $v_{ph} \approx v_{pz}$. Pestana et al. (2012) used the same approach for 2D VTI reverse time migration (RTM), with a weaker assumption $\frac{v_{ph}^2 - v_{sz}^2}{v_{pz}^2 - v_{sz}^2} \approx$ constant, where v_{sz} is the vertical S-wave phase velocity. A better approach to obtain the pure P-wave equation in TI media is proposed by Stovas et al. (2020). The idea is to set S-wave velocity in all the propagating directions to be zero in the coupled P-SV dispersion relations. A similar approach is also used here (Xu et al., 2020). While also free from any S-wave artifacts, the mixed space-wavenumber anellipticity term burdens computation. Li and Stovas (2021a) propose an acoustic wave equation for TI media that has a simpler form of the anellipticity term, with space and wavenumbers decoupled. This is done by manipulating the S-wave velocity such that the material properties and the wavenumbers are no longer coupled in the anellipticity term. However, the S-wave velocity is not ensured zero in all the propagating directions and this approximation accuracy might be dependent on material parameters. This method is also used by Li and Stovas (2021b) for the acoustic

approximation for orthorhombic media.

The above reviews some analytical approaches to derive a pure acoustic wave equation without coupling between space and wavenumbers. Numerical approaches can also be employed to deal with the coupled space-wavenumber problem. For instance, Song and Alkhalifah (2013) solved the acoustic wavefield for orthorhombic media using the low-rank approach directly on the P-wave wavefield extrapolator, where the original P-wave wavefield extrapolator entails a coupling between material properties (space-dependent) and wavenumbers in the mixed domain. Utilizing the low-rank approach to address the space-wavenumber problem has gained popularity in the literature (Engquist and Ying, 2009; Cheng and Fomel, 2014; Wu et al., 2019; Cheng et al., 2016; Fomel et al., 2013). The key advantage of this approach is its ability to circumvent numerical dispersion issues arising from the Laplacian operator, ensuring the absence of S-wave artifacts. However, when dealing with more intricate media, higher ranks are often necessary to achieve a sufficiently accurate approximation. This requirement arises from the fact that the rank of a matrix (wavefield extrapolator) represents its number of degrees of freedom or complexity. In more complex media, the corresponding matrix for the low-rank approximation becomes more challenging, demanding higher ranks for an adequate representation. And each rank demands one inverse Fourier transform (iFFT) in space.

Another notable numerical method is the Poynting vector method. As the dispersion relation contains operations among wavenumbers, Xu and Zhou (2014) proposed to transform the wavenumber vector $\boldsymbol{k}$ to the propagation direction vector $\boldsymbol{n}$ to re-

duce the computational complexity, where $\boldsymbol{n} = \frac{\boldsymbol{k}}{|\boldsymbol{k}|}$. And $\boldsymbol{n}$ can be computed by $\boldsymbol{n} = -\frac{\nabla p}{|\nabla p|}$ where p is the wavefield. Though the original papers by Xu and Zhou (2014) did not mention the term Poynting vector, we name it the Poynting vector method as it adopts the idea of Poynting vector to compute the phase angle, similar to Schaeken et al. (2022) for a non-reflecting wave equation. Zhang and Ohen (2022) used the same approach and only $\boldsymbol{k}$ in the auxiliary variable v_{sz} of the wave equation was converted to $\boldsymbol{n}$. The method of the Poynting vector is efficient as only the first-order derivatives are needed to compute the phase direction vector. However, the Poynting vector is not accurate for the approximation of the phase angle when the interference is strong as mentioned in Schaeken et al. (2022).

We have mentioned two famous numerical examples to solve the mixed-domain problem in the pure-P-wave equation for TI media, the low-rank approach and the Poynting method. The low-rank method is highly accurate if we keep enough ranks. But the number of iFFTs in space is dependent on the medium heterogeneity in the low-rank approach, which is not always cheap. The Poynting vector method may suffer from interference issues, though it is generally cheap. In this study, we seek a solution that remains independent of heterogeneity and is unaffected by interference. Our investigation begins with the acoustic VTI wave equation proposed by Stovas et al. (2020). The computational cost associated with the anellipticity term in the acoustic wave equation Stovas et al. (2020) is substantial using the hybrid finite-difference/pseudospectral method due to the presence of the mixed space-wavenumber term (anellipticity term). To address this, we leverage the assumption

of weak anellipticity (η) and approximate the anellipticity term using a Taylor series. This approximation effectively decouples the space-dependent material properties from the wavenumbers, eliminating the need for the low-rank approach or the Poynting vector method. Subsequently, we employ a hybrid finite-difference/pseudospectral method to solve the equation (Zhan et al., 2013). At each time step for a 2D case, only one Fast Fourier Transform (FFT) in space, two inverse Fast Fourier Transforms (iFFTs) in space, and additional spatial differentiations by the finite-difference method are required, ensuring computational efficiency. By employing this approach, we achieve a feasible cost in computational complexity while maintaining accurate and interference-free solutions.

In the Section Theory, we show how we derive the pure acoustic wave equation for VTI media first. We demonstrate that the coupled space-wavenumber term, as in the anellipticity term by Stovas et al. (2020), causes some numerical difficulties in solving the wavefield. Then the anellipticity term is approximated by the Taylor series with decoupled space and wavenumbers. We propose a new acoustic TTI wave equation based on this. In the Section Numerical Examples, the kinematics error is compared first between the proposed method and the methods by Chu et al. (2011), Zhang et al. (2011), Pestana et al. (2012) and Stovas et al. (2020). Then we present the wavefield extrapolator comparisons between the low-rank method and our approach. Following this, we show the wavefield benchmark, between the proposed method and those methods (Alkhalifah, 2000; Zhang and Ohen, 2022), for the homogeneous Greenhorn shale. We also use a wedge model and a checkerboard model with multiple

sources to test the stability and accuracy of our proposed method and that of Zhang and Ohen (2022). Following are some applications, such as RTM for a 2D modified Hess model and wavefield simulation and RTM for a modified 3D EAGE/SEG Salt model. Following this we discuss the importance of performing the space-wavenumber separation, the advantage of our proposed equation, and the necessity of including TTI anisotropic parameters in RTM.

THEORY

A 2D acoustic VTI medium

We recall the 2D VTI elastic velocity-stress P-SV Christoffel wave equation in x_h-x_3 plane, symmetry axis parallel to x_3-direction, and in (ω,$\boldsymbol{k}$) domain (Carcione, 2007),

$$-\mathbb{i}\omega \boldsymbol{u}(\omega, \boldsymbol{k}) = W \boldsymbol{u}(\omega, \boldsymbol{k}) \ , \tag{1}$$

where

$$\begin{aligned} \boldsymbol{u} &= \begin{bmatrix} \sigma_{hh} & \sigma_{33} & \sigma_{h3} & v_h & v_3 \end{bmatrix}^T \ , \\ W &= \begin{bmatrix} 0 & 0 & 0 & C_{11}\mathbb{i}k_h & C_{13}\mathbb{i}k_3 \\ 0 & 0 & 0 & C_{13}\mathbb{i}k_h & C_{33}\mathbb{i}k_3 \\ 0 & 0 & 0 & C_{44}\mathbb{i}k_3 & C_{44}\mathbb{i}k_h \\ \frac{1}{\rho}\mathbb{i}k_h & 0 & \frac{1}{\rho}\mathbb{i}k_3 & 0 & 0 \\ 0 & \frac{1}{\rho}\mathbb{i}k_3 & \frac{1}{\rho}\mathbb{i}k_h & 0 & 0 \end{bmatrix} \ , \end{aligned} \tag{2}$$

where ρ is the material density; C_{ij} is the material stiffness; σ_{ij} is the stress; v_i is the particle velocity; $\boldsymbol{k} = [k_h \ k_3]^T$ is the wavenumber; $\mathbb{i}^2 = -1$.

As equation 1 has a non-zero solution for $\boldsymbol{u}$, we have the following characteristic equation,

$$\det(W + \mathbb{i}\omega I) = 0 \ . \tag{3}$$

Equation 3 can be written in the following form,

$$f = v^4 + bv^2 + c = 0 \ , \tag{4}$$

with $v = \frac{\omega}{|\boldsymbol{k}|}$ being the phase velocity and $|\boldsymbol{k}|^2 = k_h^2 + k_3^2$.

Equation 4 has two solutions relative to v^2, corresponding to P- and SV-wave modes,

$$v^2 = \frac{-b \pm \sqrt{b^2 - 4c}}{2} \ , \tag{5}$$

This is the exact solution of the phase velocities and the sign + is for P-wave and − for SV-wave.

Now we introduce the density normalized stiffness, $A_{ij} = \frac{C_{ij}}{\rho}$, and

$$\eta = \frac{(A_{11} - A_{44})(A_{33} - A_{44}) - (A_{13} + A_{44})^2}{2\left((A_{33} - A_{44})A_{44} + (A_{13} + A_{44})^2\right)} \ . \tag{6}$$

Then we can parameterize equation 4 in A_{11}, A_{33}, A_{44} and η with

$$\begin{aligned} b &= -[(A_{11} + A_{44})n_h^2 + (A_{33} + A_{44})n_3^2] \ , \\ c &= A_{11}A_{44}n_h^4 + \left(\frac{A_{11}A_{44} + 2\eta A_{11}A_{33}}{1 + 2\eta} + A_{33}A_{44}\right) n_h^2 n_3^2 + A_{33}A_{44}n_3^4 \ , \end{aligned} \tag{7}$$

with $n_h = \cos(\theta) = \frac{k_h}{|\boldsymbol{k}|}$, $n_3 = \sin(\theta) = \frac{k_3}{|\boldsymbol{k}|}$ and θ being the angle between the propagating direction and x_3-direction, counterclockwise. One classic analytical acoustic approximation (Alkhalifah, 2000) corresponds to $A_{44} = 0$ and contains S-wave artifacts because equation 4 still contains two wave modes, as shown in equation 5.

A better way to approximate is to set the phase velocity of the S-wave to be zero along all propagating directions (Stovas et al., 2020). As the P-wave phase velocity is weakly dependent on A_{44} (Alkhalifah, 2000; Tsvankin and Thomsen, 1994; Alkhalifah, 1998b), we can set $c(A_{44} = \tilde{A}_{44}) = 0$ and get a new $b_p = b(A_{44} = \tilde{A}_{44})$. By doing so, the new $f_p = f(A_{44} = \tilde{A}_{44})$ only has one propagating wave mode, which is the P-wave approximation. The modified f is now given in the following form,

$$f_p = v^2 + b_p = 0 \ , \tag{8}$$

with

$$\begin{aligned} b_p &= -A_{11}n_h^2 - A_{33}n_3^2 + D(n_h^2 + n_3^2) \ , \\ D &= \frac{2\eta A_{11}A_{33}n_h^2 n_3^2}{(1+2\eta)A_{11}n_h^4 + (A_{11} + (1+2\eta)A_{33})\, n_h^2 n_3^2 + (1+2\eta)A_{33}n_3^4} \ . \end{aligned} \tag{9}$$

This acoustic approximation is identical to equation 12 in Stovas et al. (2020).

With equation 9, a formulation of the wave equation can be derived for P-wave pressure $p(t, \boldsymbol{x})$

$$\frac{\partial^2 p}{\partial t^2} = A_{11}\frac{\partial^2 p}{\partial x_h^2} + A_{33}\frac{\partial^2 p}{\partial x_3^2} - D(\boldsymbol{x}, \boldsymbol{n})\nabla^2 p, \tag{10}$$

where $\boldsymbol{x} = [x_h \ x_3]^T$ is the location coordinate and $\boldsymbol{n} = [n_h \ n_3]^T$ is the phase direction vector. As the Poynting vector represents the phase direction of the dominant wavefield (Yoon et al., 2011), $\boldsymbol{n}$ can be approximated by the Poynting vector. The Poynting vector for the acoustic wave equation is defined by $\boldsymbol{s} = -\frac{\partial p}{\partial t}\nabla p$. And then, $\boldsymbol{n} \approx \frac{\boldsymbol{s}}{|\boldsymbol{s}|} = -\frac{\nabla p}{|\nabla p|}$. Since the sign of $\boldsymbol{n}$ does not affect the solution of the wavefield, Xu and Zhou (2014) used a different sign for $\boldsymbol{n}$. This method is only valid when the interference is negligible. The method has also been applied to solve the pure acoustic wave equation for TTI media (Zhang and Ohen, 2022).

Now, we will explain why the wave equation directly obtained by equation 8 is not cheap to solve by the hybrid finite-difference/pseudospectral method. We multiply k^2 on both sides of equation 8 and assign P-wave pressure $p(\omega, \boldsymbol{k})$,

$$\begin{aligned}(-\mathbb{i}\omega)^2 p =& - b_p(\mathbb{i}k)^2 p \\ =& \left(A_{11}(\mathbb{i}k_h)^2 + A_{33}(\mathbb{i}k_3)^2 - w\right) p \ ,\end{aligned} \tag{11}$$

where

$$w = \frac{2\eta A_{11} A_{33} k_h^2 k_3^2 (k_h^2 + k_3^2)}{(1+2\eta)A_{11}k_h^4 + (A_{11} + (1+2\eta)A_{33})\, k_h^2 k_3^2 + (1+2\eta)A_{33}k_3^4} \ . \tag{12}$$

Then under the assumption of weak variation of the material properties, the solution for $p(t, \boldsymbol{x})$ is,

$$\frac{\partial^2 p}{\partial t^2} = A_{11}\frac{\partial^2 p}{\partial x_h^2} + A_{33}\frac{\partial^2 p}{\partial x_3^2} - \int_{\Omega_{\boldsymbol{k}}} w(\boldsymbol{x}, \boldsymbol{k}) \mathbb{F}(p)(\boldsymbol{k}) \exp(\mathbb{i}\boldsymbol{k}\cdot\boldsymbol{x}) d\boldsymbol{k} \ , \tag{13}$$

where $\mathbb{F}$ corresponds to the fast Fourier transform in space (FFT), $\Omega_{\boldsymbol{k}}$ is the full space of $\boldsymbol{k}$, and $p(t, \boldsymbol{k}) = \mathbb{F}\left(p(t, \boldsymbol{x})\right) = \int_{\Omega_{\boldsymbol{x}}} p(t, \boldsymbol{x}) \exp(-\mathbb{i}\boldsymbol{k}\cdot\boldsymbol{x}) d\boldsymbol{x}$ where $\Omega_{\boldsymbol{x}}$ is the full space of $\boldsymbol{x}$.

The third term of this equation contains mixed $(\boldsymbol{x}, \boldsymbol{k})$ domain, and the integral operator is expensive to evaluate as generally one iFFT in space is required for each grid point.

A cheaper solution is the low-rank approximation to w and then the number of iFFTs in space is the same as the ranks. According to Song and Alkhalifah (2013), If one model exhibits serious roughness and randomness, the ranks will end up being large, thus making it computationally expensive.

An approximation to the anellipticity term

In this study, we choose the hybrid finite-difference/pseudospectral method. As of now, the only numerical difficulty is caused by w on the right-hand-side of equation 13, which is a function of coupled space ($\boldsymbol{x}$) and wavenumber ($\boldsymbol{k}$). We aim to decouple space-dependent material properties and wavenumbers in w so that

$$\begin{aligned}
&\int_{\Omega_{\boldsymbol{k}}} w(\boldsymbol{x},\boldsymbol{k})\mathbb{F}(p)(\boldsymbol{k})\exp(\mathbb{i}\boldsymbol{k}\cdot\boldsymbol{x})d\boldsymbol{k} \\
\approx &\int_{\Omega_{\boldsymbol{k}}} \sum_{i}^{N} w_{1i}(\boldsymbol{x})w_{2i}(\boldsymbol{k})\mathbb{F}(p)(\boldsymbol{k})\exp(\mathbb{i}\boldsymbol{k}\cdot\boldsymbol{x})d\boldsymbol{k} \\
= &\sum_{i}^{N} w_{1i}(\boldsymbol{x})\int_{\Omega_{\boldsymbol{k}}} w_{2i}(\boldsymbol{k})\mathbb{F}(p)(\boldsymbol{k})\exp(\mathbb{i}\boldsymbol{k}\cdot\boldsymbol{x})d\boldsymbol{k} \\
= &\sum_{i}^{N} w_{1i}(\boldsymbol{x})\mathbb{F}^{-1}\left(w_{2i}(\boldsymbol{k})\mathbb{F}(p)(\boldsymbol{k})\right) \ ,
\end{aligned} \tag{14}$$

where $\boldsymbol{w_1} = [w_{11}\ w_{12}\ ...\ w_{1N}]^T$ only contains material properties, varying with space; $\boldsymbol{w_2} = [w_{21}\ w_{22}\ ...\ w_{2N}]^T$ only contains wavenumbers; $\mathbb{F}^{-1}$ corresponds to iFFT in space; N is the number of separated terms, as well as the number of the iFFTs required at each time step. The operation in equation 14 is indicating in equation 9,

$$D(\boldsymbol{x},\boldsymbol{n})(n_h^2+n_3^2) \approx \sum_{i}^{N} D_{1i}(\boldsymbol{x})D_{2i}(\boldsymbol{n}) \ . \tag{15}$$

In this study, we achieve the approximation in equation 15 using Taylor series under the assumption of weak anisotropy. This is equivalent to decoupling $\boldsymbol{x}$ and $\boldsymbol{k}$ in equation 14 analytically. The corresponding numerical method for the acoustic wave equation will depend on the material heterogeneity.

We construct a functional to approximate $D(\boldsymbol{x},\boldsymbol{k})(n_h^2+n_3^2)$ in equation 9,

$$g(h_1,h_2,h_3)=\frac{q_4 n_h^2 n_3^2(n_h^2+n_3^2)}{h_1 n_h^4+h_2 n_h^2 n_3^2+h_3 n_3^4}\ , \tag{16}$$

where $q_4=2\eta A_{11}A_{33}$. Then

$$\begin{aligned}
D(\boldsymbol{x},\boldsymbol{n})(n_h^2+n_3^2) =& g(q_1,q_2,q_3)\\
\approx& g(q_5,2q_5,q_5)\\
&+\frac{\partial g(q_5,2q_5,q_5)}{\partial h_1}(q_1-q_5)+\frac{\partial g(q_5,2q_5,q_5)}{\partial h_2}(q_2-2q_5)\\
&+\frac{\partial g(q_5,2q_5,q_5)}{\partial h_3}(q_3-q_5)\\
=&\frac{q_4}{q_5}\frac{n_h^2 n_3^2}{n_h^2+n_3^2}\\
&+\frac{q_4(q_5-q_1)}{q_5^2}\frac{n_h^6 n_3^2}{(n_h^2+n_3^2)^3}\\
&+\frac{q_4(2q_5-q_2)}{q_5^2}\frac{n_h^4 n_3^4}{(n_h^2+n_3^2)^3}+\frac{q_4(q_5-q_3)}{q_5^2}\frac{n_h^2 n_3^6}{(n_h^2+n_3^2)^3}\\
=&\sum_i^N D_{1i}(\boldsymbol{x})D_{2i}(\boldsymbol{n})\ ,
\end{aligned} \tag{17}$$

where $q_1=(1+2\eta)A_{11}$, $q_2=A_{11}+(1+2\eta)A_{33}$, $q_3=(1+2\eta)A_{33}$, q_5 is a scalar to be chosen, $N=4$, $D_{11}=\frac{q_4}{q_5}$, $D_{12}=\frac{q_4(q_5-q_1)}{q_5^2}$, $D_{13}=\frac{q_4(2q_5-q_2)}{q_5^2}$, $D_{14}=\frac{q_4(q_5-q_3)}{q_5^2}$, $D_{21}=\frac{n_h^2 n_3^2}{n_h^2+n_3^2}$, $D_{22}=\frac{n_h^6 n_3^2}{\left(n_h^2+n_3^2\right)^3}$, $D_{23}=\frac{n_h^4 n_3^4}{\left(n_h^2+n_3^2\right)^3}$, and $D_{24}=\frac{n_h^2 n_3^6}{\left(n_h^2+n_3^2\right)^3}$. It is found that $q_5=q_3$ results in a low approximation error. An additional advantage of doing this is that this canceled the last term in equation 17, which reduces the computational burden. Equation 17 successfully separates material properties and wave propagation directions, which means the condition of equation 14 is fullfiled when equation 17 is transformed into a wave equation. Now the P-wave kinematics with linearized

anellipticity term is

$$\begin{aligned} v^2 =& A_{11}n_h^2 + A_{33}n_3^2 \\ &- \frac{q_4}{q_5}\frac{n_h^2 n_3^2}{n_h^2+n_3^2} - \frac{q_4(q_5-q_1)}{q_5^2}\frac{n_h^6 n_3^2}{(n_h^2+n_3^2)^3} \\ &- \frac{q_4(2q_5-q_2)}{q_5^2}\frac{n_h^4 n_3^4}{(n_h^2+n_3^2)^3}\ . \end{aligned} \tag{18}$$

We can then transform equation 18 back to the $(t, \boldsymbol{x})$ domain to get the corresponding acoustic wave equation,

$$\begin{aligned} \frac{\partial^2 p}{\partial t^2} =& A_{11}\frac{\partial^2 p}{\partial x_h^2} + A_{33}\frac{\partial^2 p}{\partial x_3^2} \\ &+ \frac{q_4}{q_5}\frac{\partial^4}{\partial x_h^2 \partial x_3^2}F_1 \\ &+ \frac{q_4(q_5-q_1)}{q_5^2}\frac{\partial^8}{\partial x_h^6 \partial x_3^2}F_2 \\ &+ \frac{q_4(2q_5-q_2)}{q_5^2}\frac{\partial^8}{\partial x_h^4 \partial x_3^4}F_2 \end{aligned} \tag{19}$$

where $F_1 = \mathbb{F}^{-1}\left(\frac{1}{k_h^2+k_3^2}\mathbb{F}(p)\right)$ and $F_2 = \mathbb{F}^{-1}\left(\frac{1}{(k_h^2+k_3^2)^3}\mathbb{F}(p)\right)$.

Equation 19 is our proposed acoustic wave equation for a VTI medium. The spatial dependency and wavenumbers are decoupled. $q_i (i \in \{1, 2, ..., 5\}$ only contains material properties. The wavenumber components are merged into the spatial derivatives, F_1 and F_2. This separation is based on the above Taylor series, performing competitive accuracy compared to some existing acoustic approximations for VTI media in the later accuracy analysis. It is also beneficial for the hybrid finite-difference/pseudospectral method due to the decoupled material properties and wavenumber components.

An acoustic TTI medium

With equation 18, one can approximate the acoustic kinematics in weakly anelliptic VTI media. Now we can expand it to a generalized TTI media by

$$\begin{bmatrix} n_h \\ n_3 \end{bmatrix} \rightarrow \begin{bmatrix} \cos(\alpha) & -\sin(\alpha) \\ \sin(\alpha) & \cos(\alpha) \end{bmatrix} \begin{bmatrix} n_h \\ n_3 \end{bmatrix} , \tag{20}$$

where α is the counterclockwise rotation angle of the symmetry axis of the TI media relative to the positive x_3-axis.

One can apply the transform in equation 20 to equation 18 and obtain the approximated P-wave kinematics for a TTI medium,

$$\begin{aligned} v^2 = & \left(A_{11}\cos^2(\alpha) + A_{33}\sin^2(\alpha)\right) n_h^2 \\ & + \left(A_{33}\sin(2\alpha) - A_{11}\sin(2\alpha)\right) n_h n_3 \\ & + \left(A_{33}\cos^2(\alpha) + A_{11}\sin^2(\alpha)\right) n_3^2 \\ & + \frac{\left(q_4 - q_4\,\cos\left(4\,\alpha\right)\right)}{8q_3}\frac{n_1^4}{n_h^2+n_3^2} \\ & + \frac{4\,q_4\,\sin\left(4\,\alpha\right)}{8q_3}\frac{n_h^3 n_3}{n_h^2+n_3^2} \\ & + \frac{2\,q_4 + 6\,q_4\,\cos\left(4\,\alpha\right)}{8q_3}\frac{n_h^2 n_3^2}{n_h^2+n_3^2} \\ & - \frac{4\,q_4\,\sin\left(4\,\alpha\right)}{8q_3}\frac{n_h n_3^3}{n_h^2+n_3^2} \\ & + \frac{q_4 - q_4\,\cos\left(4\,\alpha\right)}{8q_3}\frac{n_4^4}{n_h^2+n_3^2} \\ & + \sum_{i=1}^{9} Q_i \frac{n_1^{9-i} n_3^{i-1}}{\left(n_h^2+n_3^2\right)^3} , \end{aligned} \tag{21}$$

where $Q_i (i \in \{1, 2, ..., 9\})$ are given in Appendix A and they are only functions of space.

Equation 21 corresponds to a wave equation,

$$
\begin{aligned}
\frac{\partial^2 p}{\partial t^2} = & \left(A_{11}\cos^2(\alpha) + A_{33}\sin^2(\alpha)\right)\frac{\partial^2 p}{\partial x_h^2} \\
& + \left(A_{33}\sin(2\alpha) - A_{11}\sin(2\alpha)\right)\frac{\partial^2 p}{\partial x_h \partial x_3} \\
& + \left(A_{33}\cos^2(\alpha) + A_{11}\sin^2(\alpha)\right)\frac{\partial^2 p}{\partial x_3^2} \\
& + \frac{\left(q_4 - q_4\,\cos\left(4\,\alpha\right)\right)}{8q_3^4}\frac{\partial^4 F_1}{\partial x_h^4} \\
& + \frac{4\,q_4\,\sin\left(4\,\alpha\right)}{8q_3^4}\frac{\partial^4 F_1}{\partial x_h^3 \partial x_3} \\
& + \frac{2\,q_4 + 6\,q_4\,\cos\left(4\,\alpha\right)}{8q_3^4}\frac{\partial^4 F_1}{\partial x_h^2 \partial x_3^2} \\
& - \frac{4\,q_4\,\sin\left(4\,\alpha\right)}{8q_3^4}\frac{\partial^4 F_1}{\partial x_h \partial x_3^3} \\
& + \frac{q_4 - q_4\,\cos\left(4\,\alpha\right)}{8q_3^4}\frac{\partial^4 F_1}{\partial x_3^4} \\
& + \sum_{i=1}^{9} Q_i \frac{\partial^8 F_2}{\partial x_h^{9-i}\partial x_3^{i-1}}\ .
\end{aligned}
\tag{22}
$$

Equation 22 is the acoustic wave equation for TTI media we propose in this paper. In the numerical solution, the spatial derivatives can be discretized by the finite-difference method. The 9-point centered finite-difference scheme is used for each spatial direction, regardless of the derivative order. Then the mixed space derivatives can be constructed based on the scheme. We use a 3-point centered finite-difference scheme for time discretization. The evaluations for F_1 and F_2 require one FFT and two iFFTs in space. Thus, to solve equation 19, one needs the hybrid finite-difference/pseudospectral method.

To extend equation 22 to 3D, there are 3 steps: (1) We substitute $n_h^2 = n_1^2 + n_2^2$ into equation 18, where 1 and 2 are the x_1- and x_2- directions in 3D. As such, the 2D

kinematics for a VTI medium of our proposed method is extended to 3D. (2) Another rotation transform is needed to derive the acoustic TTI kinematics,

$$\begin{bmatrix} n_1 \\ n_2 \\ n_3 \end{bmatrix} \rightarrow \begin{bmatrix} \cos(\alpha) & 0 & \sin(\alpha) \\ 0 & 1 & 0 \\ -\sin(\alpha) & 0 & \cos(\alpha) \end{bmatrix} \begin{bmatrix} \cos(\beta) & -\sin(\beta) & 0 \\ \sin(\beta) & \cos(\beta) & 0 \\ 0 & 0 & 1 \end{bmatrix} \begin{bmatrix} n_1 \\ n_2 \\ n_3 \end{bmatrix}, \tag{23}$$

where β is the azimuth angle relative to positive x_2-axis, counterclockwise. (3) The 3D acoustic TTI wave equation can be obtained using the same procedure as the 2D case. However, an explicit 3D acoustic TTI equation is not provided due to the inherent complexity involved in its expression. A 3D example including wavefield simulation and RTM is given in Appendix B.

At each time step, the finite-difference scheme expands the computational domain 4 grids in all of the directions and the pseudospectral method expands the computational grids infinitely in space. So, the bottom line of the stability is dependent on the finite-difference method. According to Kelly et al. (1976) and Alkhalifah (2000), the Courant-Friedrichs-Lewy (CFL) condition of our hybrid finite-difference/pseudospectral is $\frac{\sqrt{2}\max(v)\Delta t}{4\min(\Delta x_h,\Delta x_3)} < 1$ for 2D and $\frac{\sqrt{3}\max(v)\Delta t}{4\min(\Delta x_1,\Delta x_2,\Delta x_3)} < 1$ for 3D, where Δt is the time grid spacing and $\Delta x_i\,(i \in \{h,1,2,3\})$ is the spatial grid spacing.

The true 2D acoustic TTI solution

For benchmarking, we also need to compare our proposed method and some existing methods together with the exact solution of the acoustic TTI wavefield. We start from equation 5 with sign + for P-wave mode. Plugging equation 20 into equation 5,

we obtain the exact solution of the acoustic TTI kinematics. Similar to the process to obtain our proposed TTI acoustic wave equation, the acoustic TTI wave equation for the exact solution is derived. The exact solution of $p(t, \boldsymbol{x})$ is given by,

$$\frac{\partial^2 p}{\partial t^2} = \int_{\Omega_{\boldsymbol{k}}} H(\boldsymbol{x}, \boldsymbol{k}) \mathbb{F}(p)(\boldsymbol{k}) \exp(\mathbb{i}\boldsymbol{k} \cdot \boldsymbol{x}) d\boldsymbol{k} \ , \tag{24}$$

where

$$\begin{aligned}
H =& \frac{\tilde{b} - \sqrt{\tilde{b}^2 - 4\tilde{c}}}{2} \ , \\
\tilde{b} =& - \left((A_{11} + A_{44})(k_h \cos(\alpha) - k_3 \sin(\alpha))^2 + (A_{33} + A_{44})(k_h \sin(\alpha) + k_3 \cos(\alpha))^2 \right) \ , \\
\tilde{c} =& A_{11} A_{44} (k_h \cos(\alpha) - k_3 \sin(\alpha))^4 + \left(\frac{A_{11} A_{44} + 2\eta A_{11} A_{33}}{1 + 2\eta} + A_{33} A_{44} \right) \\
& (k_h \cos(\alpha) - k_3 \sin(\alpha))^2 (k_h \sin(\alpha) + k_3 \cos(\alpha))^2 + A_{33} A_{44} (k_h \sin(\alpha) + k_3 \cos(\alpha))^4 \ ,
\end{aligned} \tag{25}$$

In an arbitrary medium, an iFFT in space is required for each grid point of $\boldsymbol{x}$. However, normally, there are some grid points with the same material properties, and only one iFFT in space is needed for the region with identical material properties. Equation 24 is used for the exact wavefield in the numerical examples. H is the wavefield extrapolator and can be used for accuracy analysis (Details given in Numerical Examples).

NUMERICAL EXAMPLES

A VTI kinematics benchmark

We initiated our study by examining the P-wave kinematics as defined in equation 18. To provide comprehensive comparisons, we referenced several other works (Stovas

et al., 2020; Chu et al., 2011; Zhang et al., 2011; Pestana et al., 2012). In particular, we adopted equation 12 from Stovas et al. (2020), equation 20 from Chu et al. (2011), equation 14 from Zhang et al. (2011), and equation 22 from Pestana et al. (2012) for calculating P-wave phase velocities, aligning our methodology with these established references. Equation 18 offers our solution for the P-wave phase velocity in VTI media.

Greenhorn shale (Jones and Wang, 1981) is used to benchmark the accuracy of the kinematics of our proposed solution and some other solutions (Figure 1). It is shown that our proposed solution has an accuracy similar to that proposed by Stovas et al. (2020), both of which perform better than the solution by Pestana et al. (2012), Chu et al. (2011), and Zhang et al. (2011).

[Figure 1 about here.]

We further test the proposed phase velocity solution for 1000 randomly generated samples. The relative errors along all directions are stacked over those samples (Figure 2). It is found that our proposed method retains high accuracy among the other compared methods.

[Figure 2 about here.]

A wavefield extrapolator comparison to the low-rank approach

The example in this subsection illustrates a wavefield extrapolator comparison between our approach and the low-rank method. We have selected a velocity model

with varying properties along the x_3-axis (see Figure 3). Solving for the true acoustic wavefield in a general heterogeneous TTI medium is infeasible, so we focus on computing the wavefield extrapolator H at specific locations (Figure 4), as defined by equation 24.

In our experiment, we set the rank to 4 for both $\boldsymbol{x}$ and $\boldsymbol{k}$ (Fomel et al., 2013). The rank was adjusted until the low-rank approximation demonstrated performance comparable to our proposed method: the maximum absolute value of the relative error for both methods falls within a similar magnitude. Figure 4 shows the accuracy of the wavefield extrapolator by our proposed method and the low-rank method. The relative error is computed using $\frac{H_{app}-H_{true}}{|H_{true}|}$, where H_{app} is an approximation of the wavefield extrapolator H and H_{true} is the true solution. Our proposed method evidently outperforms the low-rank approach at shallower depths but becomes less competitive at greater depths. For solving the corresponding wavefields by the two methods, 4 iFFTs are necessary in the low-rank approximations, and only 2 iFFTs are needed in our proposed method.

[Figure 3 about here.]

[Figure 4 about here.]

A wavefield test for the Greenhorn shale

We assessed the accuracy of wavefield simulations in a homogeneous medium comprising Greenhorn shale, comparing our method to other existing approaches (Alkhalifah,

2000; Zhang and Ohen, 2022). In Figure 5, it is evident that all methods provide accurate approximations of the acoustic wavefield, except for the case in Figure 5 from Alkhalifah (2000), which exhibits S-wave artifacts. While S-wave artifacts are typically minor in scenarios where the source is located in a weakly anelliptic medium, eliminating them remains vital for stable acoustic wavefield simulations in TTI media with varying tilt angles (α). Our proposed method, as depicted in Figure 6, showcases the highest accuracy for this particular profile.

[Figure 5 about here.]

[Figure 6 about here.]

A wedge model

To demonstrate the stability of our proposed TTI acoustic wave equations under varying α and negative η, we generated wavefields for a wedge-shaped medium and compared our method to Zhang and Ohen (2022). The acoustic TTI wavefield derived from Alkhalifah (2000) is not shown due to instability. The wedge medium is depicted in Figure 7 and contains negative η (see Figure 7a).

Figure 8 shows that both our method and the approach by Zhang and Ohen (2022) maintain stable solutions on this wedge model, even in the presence of negative η and rapid changes in α. The shot gathers in Figure 9 also demonstrate that both of the two approximations are reliable while our proposed method is more accurate than Zhang and Ohen (2022) according to 9d.

We also benchmarked computational time for this model, using a spatial discretization of 200x200 and 5000 time steps. On a workstation with an AMD EPYC 7302P CPU and 128 GB RAM, Zhang and Ohen (2022) took 91 seconds per shot, while our proposed method required 103 seconds. The method by Zhang and Ohen (2022) proves slightly more time-efficient.

[Figure 7 about here.]

[Figure 8 about here.]

[Figure 9 about here.]

An interference test

As previously mentioned, the Poynting vector provides an approximation of the dominant phase directions for the acoustic wavefield. Methods such as Zhang and Ohen (2022) and Xu and Zhou (2014) may lack accuracy when interference is strong. In this test, we demonstrate that our method is not affected by this issue.

We created a scenario where three sources were simultaneously activated (referred to as p for this case). The wavefield was calculated for each source and then stacked together as p_{sta}. When interference does not affect the solution, p_{sta} equals p. We conducted this experiment using the model shown in Figure 10, where the three sources can induce wavefield interference.

We compared our proposed method with one of the Poynting methods, Zhang and Ohen (2022). Figure 11 displays the shot gather, showcasing both p and p_{sta}. Generally, both methods yield similar wavefield solutions. However, a slight interference issue is observed in Figure 11f for Zhang and Ohen (2022), whereas our proposed method demonstrates identical seismograms for p and p_{sta}.

[Figure 10 about here.]

[Figure 11 about here.]

An application to 2D RTM

To show the reliability of the proposed equation, we use a modified TTI version of the Hess model (Figure 12). The imaging condition is calculated using

$$I(\boldsymbol{x}) = \frac{1}{N_s} \sum_{i=1}^{N_s} \frac{\int_{\Omega_t} p_u^i(\boldsymbol{x}, t) p_d^i(\boldsymbol{x}, t) dt}{\int_t p_d^i(\boldsymbol{x}, t)^2} \ , \tag{26}$$

where I is the reflectivity image; Ω_t is the full space of t; s is the source index; N_s is the source numbers; p_u is the upgoing wavefield and p_d is the downgoing wavefield. The wavefield must be simulated until the wave energy populates all simulation grids to ensure the zero division problem in the imaging condition. The observed data is computed using our proposed acoustic TTI equation from the model in Figure 12. For TTI RTM, both p_d and p_u are calculated using the model in Figure 12, but $\alpha = 0$ for VTI RTM and $\eta = 0$ for elliptic RTM.

[Figure 12 about here.]

Figure 13b displays the migration results. To evaluate the significance of the tilt angle (Figure 13c) and anellipticity (Figure 13d), we introduced several imperfections in the migration process. For reference, Figure 13a represents the vertical differentiation of the model A_{33}, revealing the true interfaces.

Notably, the TI migration in Figure 13b produces the clearest image. However, due to inaccurate wavefield simulations, Figures 13c and 13d exhibit more migration noise and a loss of reflector accuracy.

Another example including wavefield simulation and RTM for the modified 3D EAGE/SEG Salt model is given in Appendix B.

[Figure 13 about here.]

DISCUSSIONS

We propose a new acoustic TTI wave equation. We start from the acoustic approximation by Stovas et al. (2020) for VTI media. The Christoffel equation of the new acoustic wave equation only contains the P-wave propagating mode, so it lacks S-wave artifacts. However, the acoustic wave equation by Stovas et al. (2020) has a coupled ($\boldsymbol{x}$,$\boldsymbol{k}$) anellipticity term, so it is not cheap to solve with the hybrid finite-difference/pseudospectral method. A treatment of the anellipticity term using Taylor series can decouple the space and wavenumber dependencies analytically, then the hybrid finite-difference/pseudospectral method can be applied. For a 2D case, only one FFT in space, two iFFTs in space, and additional spatial differentiations using the

finite-difference method are required at each time step. This method is not dependent on media heterogeneity and is not prone to wavefield interference.

In the kinematics analysis and the wavefield extrapolator comparison, we show that our proposed method has a competitive accuracy. Followed by the stability test of a wedge model and the interference test, our proposed method is stable under fast change of α, negative η, and is not affected by the interference issues. Those factors are key for an accurate and stable acoustic TTI wavefield simulation. We compare the computational cost of our proposed method with one of the cheap Poynting vector methods. Our proposed method is not much more expensive than the efficient Poynting vector method while retaining more accuracy in certain circumstances.

The RTM example shows the necessity to include anellipticity η and tilt angle of the symmetry axis α in seismic imaging to avoid losing information. However, including more physical properties in the method application is more computationally expensive. For instance, including the anellipticity term requires special treatment to separate the space and wavenumbers. The tilt angle of the symmetry axis complicates the spatial derivatives.

CONCLUSIONS

This paper presents a new acoustic wave equation for TTI media. Its solution does not suffer from S-wave artifacts. The equation is obtained by applying a Taylor series expansion to the anellipticity term of the existing pure P-wave equation with a rotation to the wavenumber vector. Numerically, the acoustic TTI wave equation can

be solved by the hybrid finite-difference/pseudospectral method. This method is not expensive and maintains high accuracy. The wavefield solution always appears stable and devoid of artifacts, even for challenging media with fast-changing tilt angles. The RTM for the 2D modified Hess model demonstrates the necessity of considering the ellipticity and tilt angle for the TI media. The example for the modified 3D EAGE/SEG Salt model demonstrates the method is applicable to 3D. As a result, our proposed acoustic TTI wave equation holds considerable promise for advancing seismic imaging and analysis in scenarios where Earth's subsurface exhibits the utmost complexity and variability.

ACKNOWLEDGMENTS

This work was supported by the Max Planck Graduate Center with the Johannes Gutenberg University of Mainz (MPGC). We would like to express our gratitude to the editors, Antoine Guitton, Tieyuan Zhu, Kristopher Innanen, and Alison Malcolm, as well as the reviewers Linbin Zhang, Shibo Xu, and an anonymous reviewer, for their valuable comments and helpful suggestions.

DATA AND MATERIALS AVAILABILITY

Data associated with this research are available and can be obtained by contacting the corresponding author.

APPENDIX A

COEFFICIENTS

Coefficients $Q_i (i \in \{1, 2, ..., 9\})$ in equations 21 and 22 are giben by,

$$
\begin{aligned}
Q_1 =& \frac{128}{q_3^2} \left(11\, q_3\, q_4 - 3\, q_2\, q_4 - 5\, q_1\, q_4 - \sigma_{37} + \sigma_{34} + \sigma_{33} + \sigma_{31} + \sigma_{30} - \sigma_{26} + \sigma_{36} - \sigma_{28} - \sigma_{35} + \sigma_{32}\right) \ , \\
Q_2 =& \frac{128}{q_3^2} (\sigma_{17} - \sigma_3 - \sigma_{16} - \sigma_2 - \sigma_{10} + \sigma_1 - \sigma_{15} + \sigma_9 + \sigma_{14} - \sigma_{13}) \ , \\
Q_3 =& \frac{128}{q_3^2} \left(44\, q_3\, q_4 - 12\, q_2\, q_4 - 20\, q_1\, q_4 - \sigma_{29} - \sigma_{25} + \sigma_{27} - \sigma_{24} - \sigma_{19} + \sigma_{20} - \sigma_{23} + \sigma_{18} + \sigma_{22} - \sigma_{21}\right) \ , \\
Q_4 =& \frac{128}{q_3^2} \left(\sigma_{12} - \sigma_3 - \sigma_{11} - \sigma_2 + \sigma_8 + \sigma_1 + \sigma_7 - \sigma_6 - \sigma_5 + \sigma_4\right) \ , \\
Q_5 =& \frac{128}{q_3^2} (66\, q_3\, q_4 - 18\, q_2\, q_4 - 30\, q_1\, q_4 - 40\, q_1\, q_4\, \cos(4\,\alpha) - 40\, q_2\, q_4\, \cos(4\,\alpha) + 120\, q_3\, q_4\, \cos(4\,\alpha) \\
& + 70\, q_1\, q_4\, \cos(8\,\alpha) - 70\, q_2\, q_4\, \cos(8\,\alpha) + 70\, q_3\, q_4\, \cos(8\,\alpha)) \ , \\
Q_6 =& \frac{128}{q_3^2} (\sigma_{12} + \sigma_3 - \sigma_{11} + \sigma_2 + \sigma_8 - \sigma_1 - \sigma_7 - \sigma_6 + \sigma_5 - \sigma_4) \ , \\
Q_7 =& \frac{128}{q_3^2} (44\, q_3\, q_4 - 12\, q_2\, q_4 - 20\, q_1\, q_4 + \sigma_{29} - \sigma_{25} - \sigma_{27} - \sigma_{24} + \sigma_{19} + \sigma_{20} - \sigma_{23} - \sigma_{18} + \sigma_{22} - \sigma_{21}) \ , \\
Q_8 =& \frac{128}{q_3^2} (\sigma_{17} + \sigma_3 - \sigma_{16} + \sigma_2 - \sigma_{10} - \sigma_1 + \sigma_{15} + \sigma_9 - \sigma_{14} + \sigma_{13}) \ , \\
Q_9 =& \frac{128}{q_3^2} (11\, q_3\, q_4 - 3\, q_2\, q_4 - 5\, q_1\, q_4 + \sigma_{37} + \sigma_{34} - \sigma_{33} + \sigma_{31} - \sigma_{30} - \sigma_{26} + \sigma_{36} + \sigma_{28} - \sigma_{35} + \sigma_{32}) \ ,
\end{aligned}
$$

(A-1)

where $\sigma_i (i \in \{1, 2, ..., 37\})$ are given by,

$$\sigma_1 = 48\, q_3\, q_4\, \sin(4\,\alpha)\,,\ \sigma_2 = 16\, q_2\, q_4\, \sin(4\,\alpha)\,,$$

$$\sigma_3 = 16\, q_1\, q_4\, \sin(4\,\alpha)\,,\ \sigma_4 = 56\, q_3\, q_4\, \sin(8\,\alpha)\,,$$

$$\sigma_5 = 56\, q_2\, q_4\, \sin(8\,\alpha)\,,\ \sigma_6 = 56\, q_3\, q_4\, \sin(6\,\alpha)\,,$$

$$\sigma_7 = 56\, q_1\, q_4\, \sin(8\,\alpha)\,,\ \sigma_8 = 56\, q_1\, q_4\, \sin(6\,\alpha)\,,$$

$$\sigma_9 = 24\, q_3\, q_4\, \sin(6\,\alpha)\,,\ \sigma_{10} = 24\, q_1\, q_4\, \sin(6\,\alpha)\,,$$

$$\sigma_{11} = 24\, q_3\, q_4\, \sin(2\,\alpha)\,,\ \sigma_{12} = 24\, q_1\, q_4\, \sin(2\,\alpha)\,,$$

$$\sigma_{13} = 8\, q_3\, q_4\, \sin(8\,\alpha)\,,\ \sigma_{14} = 8\, q_2\, q_4\, \sin(8\,\alpha)\,,$$

$$\sigma_{15} = 8\, q_1\, q_4\, \sin(8\,\alpha)\,,\ \sigma_{16} = 8\, q_3\, q_4\, \sin(2\,\alpha)\,,$$

$$\sigma_{17} = 8\, q_1\, q_4\, \sin(2\,\alpha)\,,\ \sigma_{18} = 56\, q_3\, q_4\, \cos(6\,\alpha)\,,$$

$$\sigma_{19} = 56\, q_1\, q_4\, \cos(6\,\alpha)\,,\ \sigma_{20} = 48\, q_3\, q_4\, \cos(4\,\alpha)\,, \qquad \text{(A-2)}$$

$$\sigma_{21} = 28\, q_3\, q_4\, \cos(8\,\alpha)\,,\ \sigma_{22} = 28\, q_2\, q_4\, \cos(8\,\alpha)\,,$$

$$\sigma_{23} = 28\, q_1\, q_4\, \cos(8\,\alpha)\,,\ \sigma_{24} = 16\, q_2\, q_4\, \cos(4\,\alpha)\,,$$

$$\sigma_{25} = 16\, q_1\, q_4\, \cos(4\,\alpha)\,,\ \sigma_{26} = 12\, q_3\, q_4\, \cos(4\,\alpha)\,,$$

$$\sigma_{27} = 8\, q_3\, q_4\, \cos(2\,\alpha)\,,\ \sigma_{28} = 4\, q_3\, q_4\, \cos(6\,\alpha)\,,$$

$$\sigma_{29} = 8\, q_1\, q_4\, \cos(2\,\alpha)\,,\ \sigma_{30} = 4\, q_1\, q_4\, \cos(6\,\alpha)\,,$$

$$\sigma_{31} = 4\, q_2\, q_4\, \cos(4\,\alpha)\,,\ \sigma_{32} = q_3\, q_4\, \cos(8\,\alpha)\,,$$

$$\sigma_{33} = 4\, q_3\, q_4\, \cos(2\,\alpha)\,,\ \sigma_{34} = 4\, q_1\, q_4\, \cos(4\,\alpha)\,,$$

$$\sigma_{35} = q_2\, q_4\, \cos(8\,\alpha)\,,\ \sigma_{36} = q_1\, q_4\, \cos(8\,\alpha)\,,$$

$$\sigma_{37} = 4\, q_1\, q_4\, \cos(2\,\alpha)\,.$$

APPENDIX B

A 3D EXAMPLE

We perform a 3D numerical experiment in this section. Our proposed 2D acoustic TTI wave equation is extended to 3D using the procedure given in Subsection An acoustic TTI medium. The EAGE/SEG Salt model is modified. As the original 3D EAGE/SEG Salt model is isotropic, we add to its complexity by introducing some anisotropic TTI parameters (Figure 14). Figure 15 is an example of the wavefield and Figure 16 is the RTM image.

[Figure 14 about here.]

[Figure 15 about here.]

[Figure 16 about here.]

REFERENCES

Alkhalifah, T., 1998a, Acoustic approximations for processing in transversely isotropic media: Geophysics, **63**.

———, 1998b, Acoustic approximations for processing in transversely isotropic media: GEOPHYSICS, **63**, 623–631.

———, 2000, An acoustic wave equation for anisotropic media: Geophysics, **65**, 1239–1250.

Carcione, J. M., 2007, Wave fields in real media: Wave propagation in anisotropic, anelastic, porous and electromagnetic media: Elsevier.

Cheng, J., T. Alkhalifah, Z. Wu, P. Zou, and C. Wang, 2016, Simulating propagation of decoupled elastic waves using low-rank approximate mixed-domain integral operators for anisotropic media: Geophysics, **81**, T63–T77.

Cheng, J., and S. Fomel, 2014, Fast algorithms for elastic-wave-mode separation and vector decomposition using low-rank approximation for anisotropic media: Geophysics, **79**, C97–C110.

Chu, C., B. K. Macy, and P. D. Anno, 2011, Approximation of pure acoustic seismic wave propagation in tti media: GEOPHYSICS, **76**, WB97–WB107.

Engquist, B., and L. Ying, 2009, A fast directional algorithm for high frequency acoustic scattering in two dimensions: Commun. Math. Sci., **7**, 327–345.

Fomel, S., L. Ying, and X. Song, 2013, Seismic wave extrapolation using lowrank symbol approximation: Geophysical Prospecting, **61**, 526–536.

Jones, L. E. A., and H. F. Wang, 1981, Ultrasonic velocities in cretaceous shales from

the williston basin: Geophysics, **46**, 288–297.

Kelly, K. R., R. W. Ward, S. Treitel, and R. M. Alford, 1976, Synthetic seismograms: A finite -difference approach: GEOPHYSICS, **41**, 2–27.

Li, B., and A. Stovas, 2021a, Decoupled approximation and separate extrapolation of p- and sv-waves in transversely isotropic media: Geophysics, **86**, C133–C142.

———, 2021b, Decoupling approximation of p- and s-wave phase velocities in orthorhombic media: Geophysics, **87**, T169–T182.

Li, Q., H. Zhou, Q. Zhang, H. Chen, and S. Sheng, 2015, Efficient reverse time migration based on fractional laplacian viscoacoustic wave equation: Geophysical Journal International, **204**, 488–504.

Pestana, R. C., B. Ursin, and P. L. Stoffa, 2012, Rapid expansion and pseudo spectral implementation for reverse time migration in vti media: Journal of Geophysics and Engineering, **9**, 291–301.

Schaeken, T., L. Hoogerbrugge, and E. Verschuur, 2022, A non-reflecting wave equation through directional wave-field suppression and its finite difference implementation: Sci Rep, **12**, 407. (Schaeken, Teun Hoogerbrugge, Leo Verschuur, Eric eng England 2022/01/12 Sci Rep. 2022 Jan 10;12(1):407. doi: 10.1038/s41598-021-04064-3.).

Song, X., and T. Alkhalifah, 2013, Modeling of pseudoacoustic p-waves in orthorhombic media with a low-rank approximation: Geophysics, **78**, 33–40.

Stovas, A., T. Alkhalifah, and U. b. Waheed, 2020, Pure p- and s-wave equations in transversely isotropic media: Geophysical Prospecting, **68**, 2762–2769.

Thomsen, L., 2002, Understanding seismic anisotropy in exploration and exploitation,

2nd ed.: Society of Exploration Geophysicists.

Tsvankin, I., 2012, Seismic signatures and analysis of reflection data in anisotropic media: Society of Exploration Geophysicists.

Tsvankin, I., and L. Thomsen, 1994, Nonhyperbolic reflection moveout in anisotropic media: GEOPHYSICS, **59**, 1290–1304.

Wu, Z., T. Alkhalifah, and Z. Zhang, 2019, A partial-low-rank method for solving acoustic wave equation: Journal of Computational Physics, **385**, 1–12.

Xu, S., A. Stovas, T. Alkhalifah, and H. Mikada, 2020, New acoustic approximation for transversely isotropic media with a vertical symmetry axis: Geophysics, **85**, C1–C12.

Xu, S., and H. Zhou, 2014, Accurate simulations of pure quasi-p-waves in complex anisotropic media: Geophysics, **79**, T341–T348.

Yang, J., and H. Zhu, 2018, Viscoacoustic reverse time migration using a time-domain complex-valued wave equation: Geophysics, 1–92.

Yoon, K., M. Guo, J. Cai, and B. Wang, 2011, *in* 3D RTM angle gathers from source wave propagation direction and dip of reflector: 3136–3140.

Zhan, G., R. C. Pestana, and P. L. Stoffa, 2013, An efficient hybrid pseudospectral/finite-difference scheme for solving the tti pure p-wave equation: Journal of Geophysics and Engineering, **10**.

Zhang, L., and E. Ohen, 2022, A stable tti acoustic wave equation: Second International Meeting for Applied Geoscience and Energy, 2527–2531.

Zhang, Y., H. Zhang, and G. Zhang, 2011, A stable tti reverse time migration and its implementation: GEOPHYSICS, **76**, WA3–WA11.

Zhou, H., G. Zhang, and R. Bloor, 2006, An anisotropic acoustic wave equation for modeling and migration in 2d tti media: SEG Technical Program Expanded Abstracts 2006, 194–198.

LIST OF FIGURES

1 The P-wave kinematics for Greenhorn shale. $A_{11} = 1.447\times10^7$ Pa m^3/kg, $A_{33} = 9.57 \times 10^6$ Pa m^3/kg, $A_{13} = 4.51 \times 10^6$ Pa m^3/kg, $A_{44} = 2.28 \times 10^6$ Pa m^3/kg, thus, $\eta = 0.3409$. (a) Exact P-wave phase velocity. (b) Relative error of the estimated P-wave phase velocity $E_r = \frac{|v_{est}-v_{exa}|}{|v_{exa}|}$, where v_{est} is the estimated solution and v_{exa} is the exact solution. 37

2 The average stacked relative error of the estimated P-wave phase velocity for randomly generated 1000 VTI samples using a uniform distribution. The stacking is performed for each phase angle. $A_{11} \sim U(1.1 \times 10^7$ Pa m^3/kg$, 1.7 \times 10^7$ Pa m^3/kg$)$, $A_{33} \sim U(7 \times 10^6$ Pa m^3/kg$, 1.25 \times 10^7$ Pa m^3/kg$)$, $A_{13} \sim U(1.5 \times 10^6$ Pa m^3/kg$, 3 \times 10^6$ Pa m^3/kg$)$, $A_{44} \sim U(3.5 \times 10^6$ Pa m^3/kg$, 4.5 \times 10^6$ Pa m^3/kg$)$. U is for uniform distribution. Thus $\eta \in [-0.2475, 0.7100]$ in our experiment. 38

3 The model for comparison to the low-rank approach, which is only a function of x_3. 39

4 The acoustic wavefield extrapolators H for the model given in Figure 3. (a) - (c) are for the location $x_h = 30$ m, $x_3 = 100$ m. (d) - (f) are for the location $x_h = 30$ m, $x_3 = 500$ m. (g) - (i) are for the location $x_h = 30$ m, $x_3 = 900$ m. (a), (d), and (g) are the true solutions. (b), (e), and (h) are the relative errors of the low-rank approach, solved with 4 ranks for $\boldsymbol{x}$ and $\boldsymbol{k}$, respectively. (c), (f), and (i) are the relative errors of our proposed solutions. 40

5 The acoustic wavefield for the Greenhorn shale at 0.5 s. The red down-pointing triangle in (a) is the source. The source signature is Ricker wavelet, 10 Hz. (a) Exact solution. (b) VTI wavefield by Alkhalifah (2000). (c) VTI wavefield by Zhang and Ohen (2022). (d) Proposed VTI solution. (e) Proposed TI solution with $\alpha = \pi/6$. 41

6 The profile at $x_h = 1600$ m for Figure 5 a-d. 42

7 The wedge model. (a) η. (b) α. The other parameters are set homogeneous along the space. $A_{11} = 1.4 \times 10^7$ Pa m^3/kg, $A_{33} = 1.0 \times 10^7$ Pa m^3/kg, $A_{44} = 2.0 \times 10^6$ Pa m^3/kg. 30 receivers are placed evenly at $x_h \in [780, 5130]$ m and $x_3 = 750m$. 43

8 The acoustic wavefield for the model in Figure 7. The source signature is a Ricker wavelet, 10 Hz. Acoustic approximations (a)(d)(g) are at 0.5 s, (b)(e)(h) at 1 s and (c)(f)(i) at 1.8 s. (a) - (c) are computed by the method of Zhang and Ohen (2022) and (d) - (f) are from our proposed method. (g) - (i) are exact solutions. 44

9 The shot gather from the wavefield in setup given in Figure 8, (a) for Zhang and Ohen (2022), (b) for proposed method, (c) for exact solution and (d) differences between the approximations and the true solution for the receiver index 25. 45

10 The checkerboard model. For white region, $A_{11} = 1.4 \times 10^7$ Pa m^3/kg, $A_{33} = 1.0 \times 10^7$ Pa m^3/kg, $A_{44} = 7 \times 10^6$ Pa m^3/kg, $\eta = 0.2$, $\alpha = \pi/3$. For the black region, the values of the above parameters are doubled. The down-pointing triangles are the source locations. 46

11 The shot gathers for Figure 10. Ricker wavelet, 10 Hz. p is the solution when 3 sources are shot simultaneously, and p_{sta} is the stacked solution for each shot wavefield, (a) p by our proposed method, (b) p_{sta} by our proposed method, (c) True seismograms for receiver index 15, (d) p by Zhang and Ohen (2022), (e) p_{sta} by Zhang and Ohen (2022), and (f) $p_{sta} - p$ for Zhang and Ohen (2022) and the proposed method. 47

12 The modified Hess model. (a) A_{11}. (b) A_{33}. (c) η. (d) An additional tilt angle α of the symmetry axis is added to the original Hess model. The down-pointing triangles are the imaging source locations. 201 receivers are placed evenly at $x_h \in [1281, 25681]$ m and $x_3 = 1342$ m. 48

13 The reflectivity images I. Source: Ricker wavelet, 4 Hz. 17 sources are placed evenly at $x_h \in [1281, 20862]$ m, $x_3 = 1342m$. The source signature is a Ricker wavelet, 2 Hz. (a) is the image derived from the vertical differentiation of A_{33}. (b)(c) and (d) are for TTI, VTI, and elliptic migration images, respectively. In (c) and (d), artifacts are marked with red arrows and reflector missing accuracies are indicated in blue 49

14 The modified 3D EAGE/SEG Salt model. We obtain our acoustic TTI model by $A_{11} = v^2$, $A_{33} = 1.4A_{11}$, $\eta = 0.2\frac{A_{11}}{max(A_{11})}$, $\alpha = \frac{\pi}{2}\frac{A_{11}}{max(A_{11})}$, $\beta = 2\pi\frac{A_{11}}{max(A_{11})}$, where v is the original velocity of 3D EAGE/SEG model. (a) Slice at $x_1 = 4400$ m. (b) Slice at $x_2 = 4400$ m. (c) Slice at $x_3 = 2800$ m. The down-pointing triangles are the imaging source locations projected on those planes. 216000 receivers are evenly distributed in this range, $x_1 \in [840, 12640]$ m, $x_2 \in [840, 12640]$ m, $x_3 = 840$ m. 50

15 The solution of the wavefield by the proposed method. The source is placed at $[4440\ 4440\ 840]^T$ m. Source: Ricker wavelet, 7 Hz. The three rows are corresponding $t = 0.3,\ 0.4,\ 0.6$ s. The three columns are corresponding to the same slices with Figure 14 for (a), (b), and (c). . 51

16 The RTM image for the model in Figure 14. Same slices with Figure 14 for (a), (b), and (c). 52

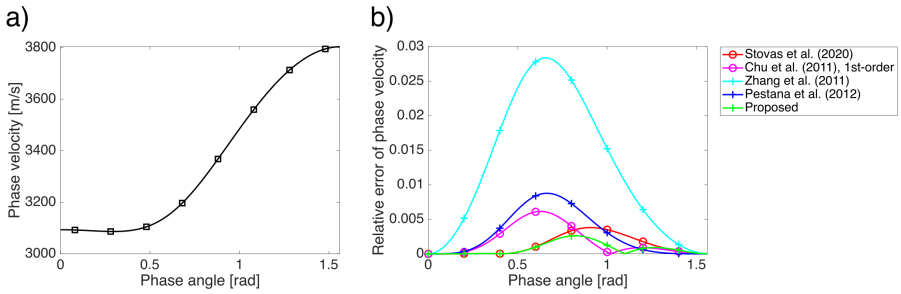

Figure 1: The P-wave kinematics for Greenhorn shale. $A_{11} = 1.447 \times 10^7$ Pa m^3/kg, $A_{33} = 9.57 \times 10^6$ Pa m^3/kg, $A_{13} = 4.51 \times 10^6$ Pa m^3/kg, $A_{44} = 2.28 \times 10^6$ Pa m^3/kg, thus, $\eta = 0.3409$. (a) Exact P-wave phase velocity. (b) Relative error of the estimated P-wave phase velocity $E_r = \frac{|v_{est} - v_{exa}|}{|v_{exa}|}$, where v_{est} is the estimated solution and v_{exa} is the exact solution.

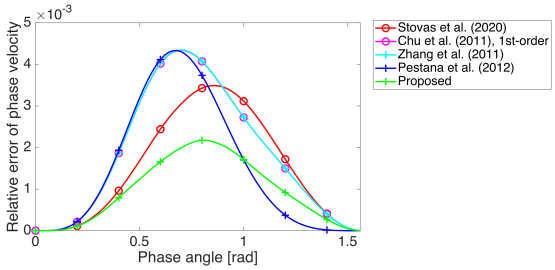

Figure 2: The average stacked relative error of the estimated P-wave phase velocity for randomly generated 1000 VTI samples using a uniform distribution. The stacking is performed for each phase angle. $A_{11} \sim U(1.1 \times 10^7$ Pa m^3/kg$, 1.7 \times 10^7$ Pa m^3/kg$)$, $A_{33} \sim U(7 \times 10^6$ Pa m^3/kg$, 1.25 \times 10^7$ Pa m^3/kg$)$, $A_{13} \sim U(1.5 \times 10^6$ Pa m^3/kg$, 3 \times 10^6$ Pa m^3/kg$)$, $A_{44} \sim U(3.5 \times 10^6$ Pa m^3/kg$, 4.5 \times 10^6$ Pa m^3/kg$)$. U is for uniform distribution. Thus $\eta \in [-0.2475, 0.7100]$ in our experiment.

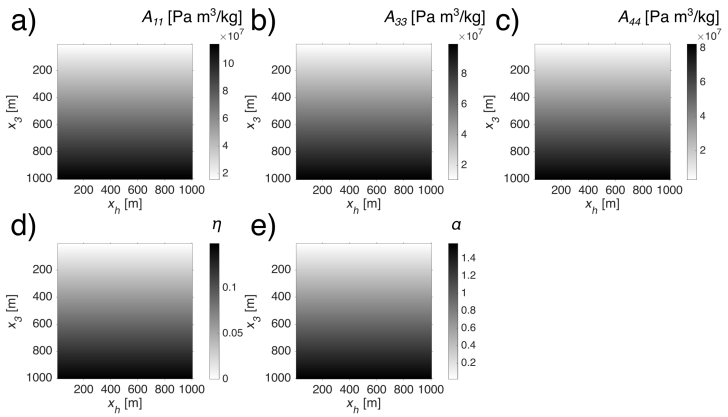

Figure 3: The model for comparison to the low-rank approach, which is only a function of x_3.

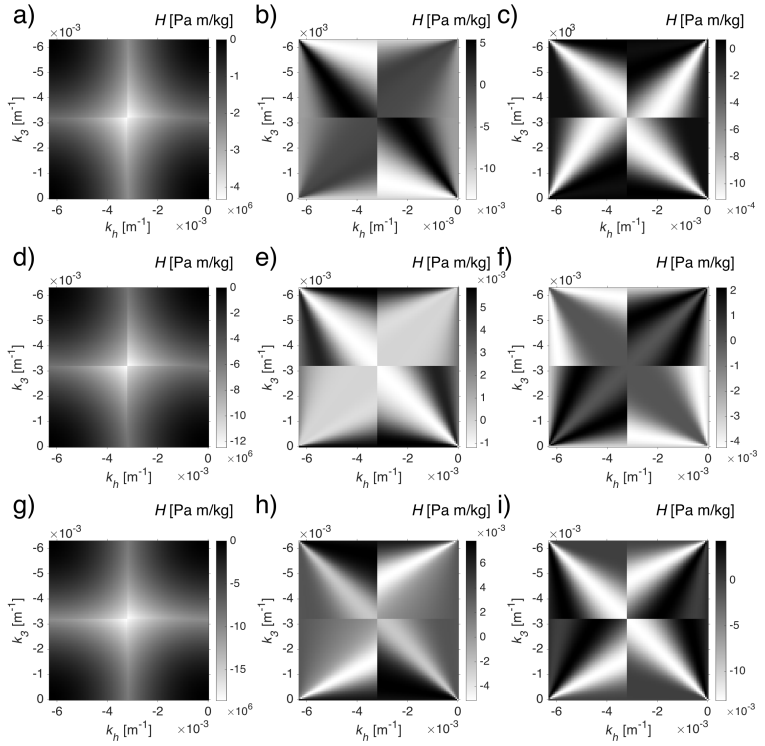

Figure 4: The acoustic wavefield extrapolators H for the model given in Figure 3. (a) - (c) are for the location $x_h = 30$ m, $x_3 = 100$ m. (d) - (f) are for the location $x_h = 30$ m, $x_3 = 500$ m. (g) - (i) are for the location $x_h = 30$ m, $x_3 = 900$ m. (a), (d), and (g) are the true solutions. (b), (e), and (h) are the relative errors of the low-rank approach, solved with 4 ranks for $\boldsymbol{x}$ and $\boldsymbol{k}$, respectively. (c), (f), and (i) are the relative errors of our proposed solutions.

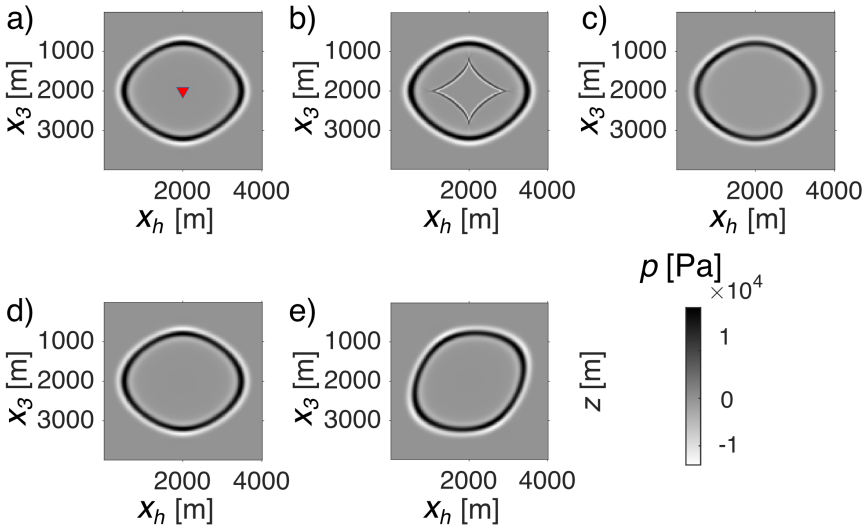

Figure 5: The acoustic wavefield for the Greenhorn shale at 0.5 s. The red down-pointing triangle in (a) is the source. The source signature is Ricker wavelet, 10 Hz. (a) Exact solution. (b) VTI wavefield by Alkhalifah (2000). (c) VTI wavefield by Zhang and Ohen (2022). (d) Proposed VTI solution. (e) Proposed TI solution with $\alpha = \pi/6$.

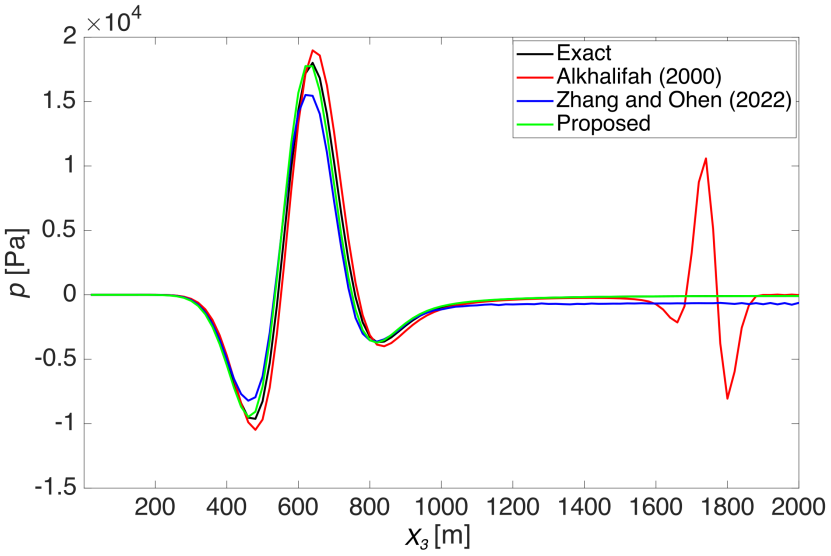

Figure 6: The profile at $x_h = 1600$ m for Figure 5 a-d.

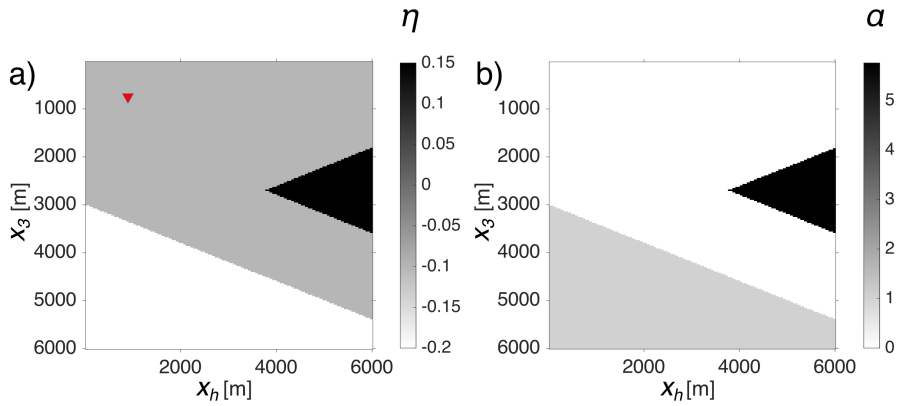

Figure 7: The wedge model. (a) η. (b) α. The other parameters are set homogeneous along the space. $A_{11} = 1.4 \times 10^7$ Pa m^3/kg, $A_{33} = 1.0 \times 10^7$ Pa m^3/kg, $A_{44} = 2.0 \times 10^6$ Pa m^3/kg. 30 receivers are placed evenly at $x_h \in [780, 5130]$ m and $x_3 = 750m$.

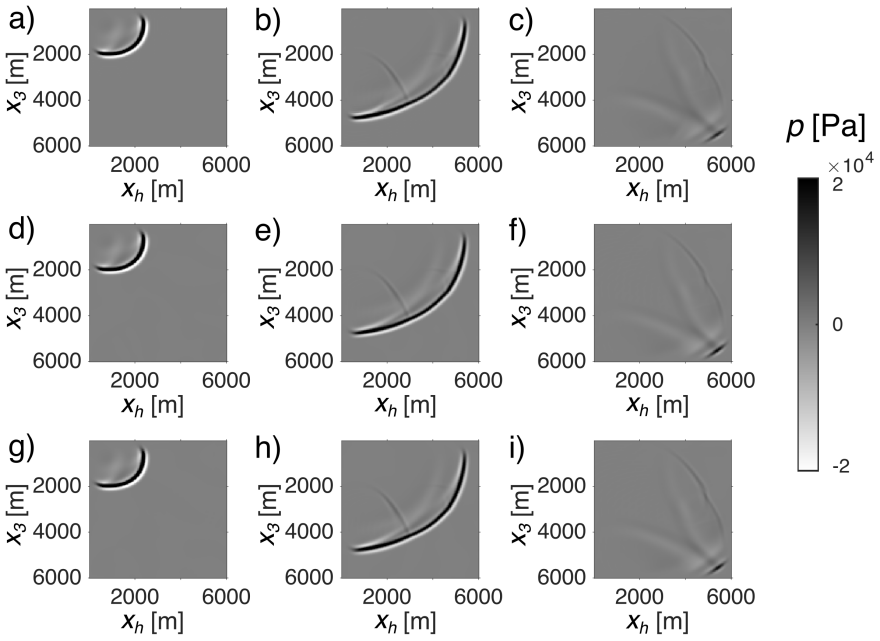

Figure 8: The acoustic wavefield for the model in Figure 7. The source signature is a Ricker wavelet, 10 Hz. Acoustic approximations (a)(d)(g) are at 0.5 s, (b)(e)(h) at 1 s and (c)(f)(i) at 1.8 s. (a) - (c) are computed by the method of Zhang and Ohen (2022) and (d) - (f) are from our proposed method. (g) - (i) are exact solutions.

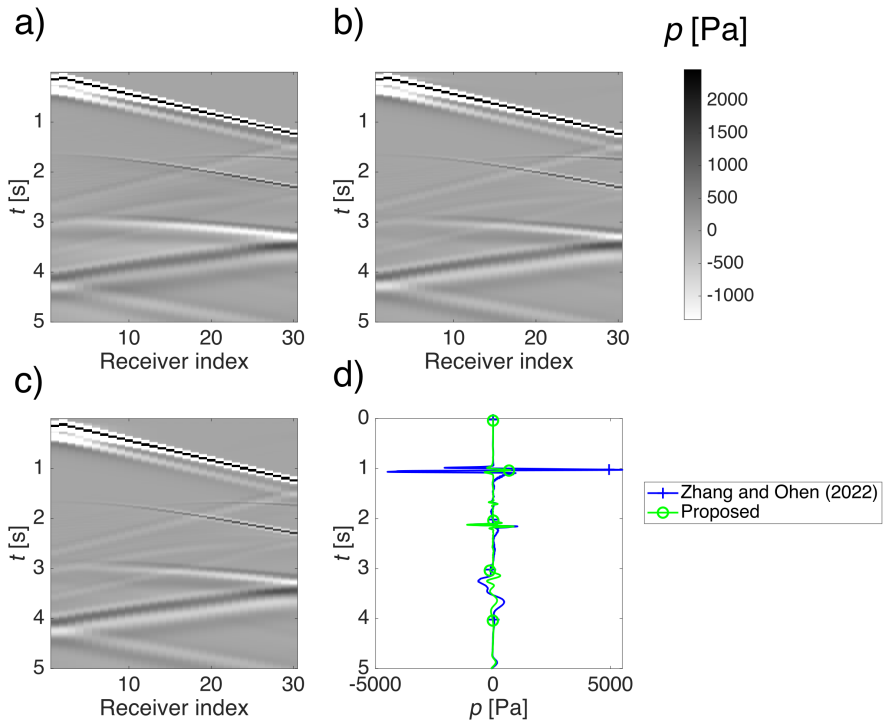

Figure 9: The shot gather from the wavefield in setup given in Figure 8, (a) for Zhang and Ohen (2022), (b) for proposed method, (c) for exact solution and (d) differences between the approximations and the true solution for the receiver index 25.

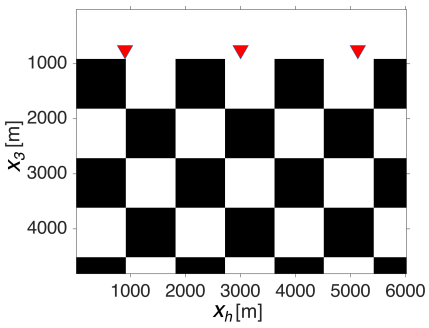

Figure 10: The checkerboard model. For white region, $A_{11} = 1.4 \times 10^7$ Pa m^3/kg, $A_{33} = 1.0 \times 10^7$ Pa m^3/kg, $A_{44} = 7 \times 10^6$ Pa m^3/kg, $\eta = 0.2$, $\alpha = \pi/3$. For the black region, the values of the above parameters are doubled. The down-pointing triangles are the source locations.

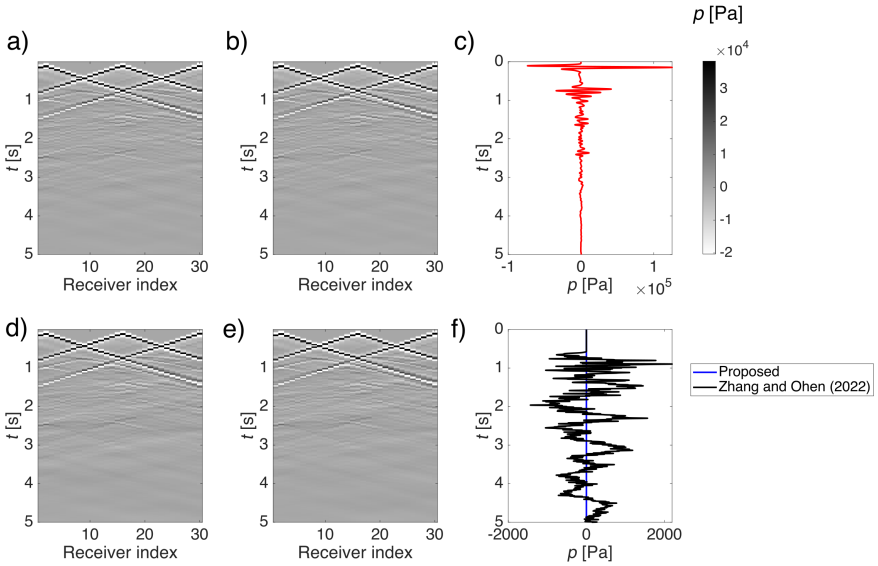

Figure 11: The shot gathers for Figure 10. Ricker wavelet, 10 Hz. p is the solution when 3 sources are shot simultaneously, and p_{sta} is the stacked solution for each shot wavefield, (a) p by our proposed method, (b) p_{sta} by our proposed method, (c) True seismograms for receiver index 15, (d) p by Zhang and Ohen (2022), (e) p_{sta} by Zhang and Ohen (2022), and (f) $p_{sta} - p$ for Zhang and Ohen (2022) and the proposed method.

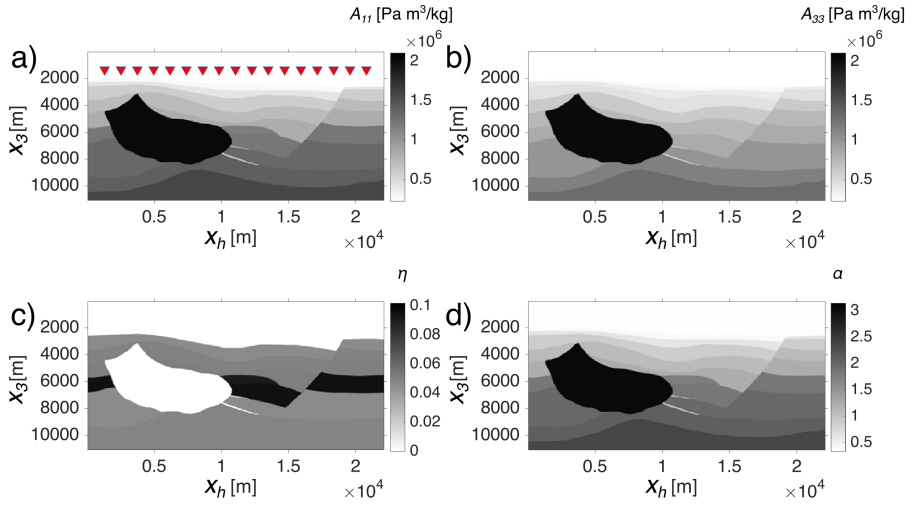

Figure 12: The modified Hess model. (a) A_{11}. (b) A_{33}. (c) η. (d) An additional tilt angle α of the symmetry axis is added to the original Hess model. The down-pointing triangles are the imaging source locations. 201 receivers are placed evenly at $x_h \in [1281, 25681]$ m and $x_3 = 1342$ m.

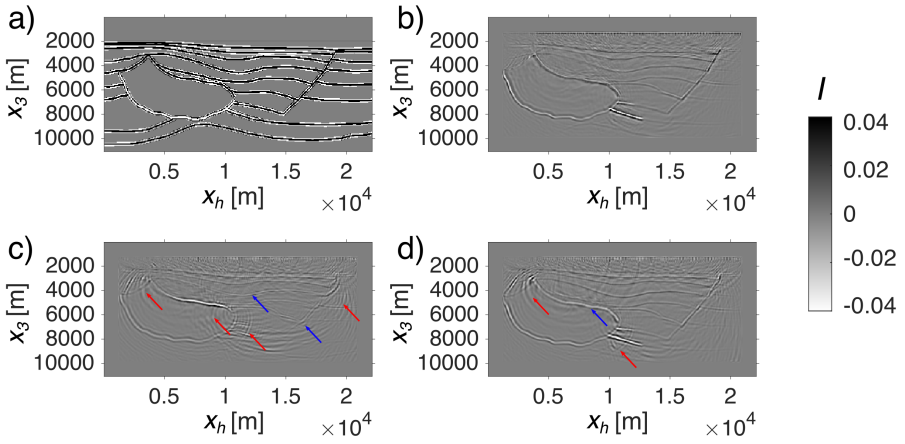

Figure 13: The reflectivity images I. Source: Ricker wavelet, 4 Hz. 17 sources are placed evenly at $x_h \in [1281, 20862]$ m, $x_3 = 1342m$. The source signature is a Ricker wavelet, 2 Hz. (a) is the image derived from the vertical differentiation of A_{33}. (b)(c) and (d) are for TTI, VTI, and elliptic migration images, respectively. In (c) and (d), artifacts are marked with red arrows and reflector missing accuracies are indicated in blue .

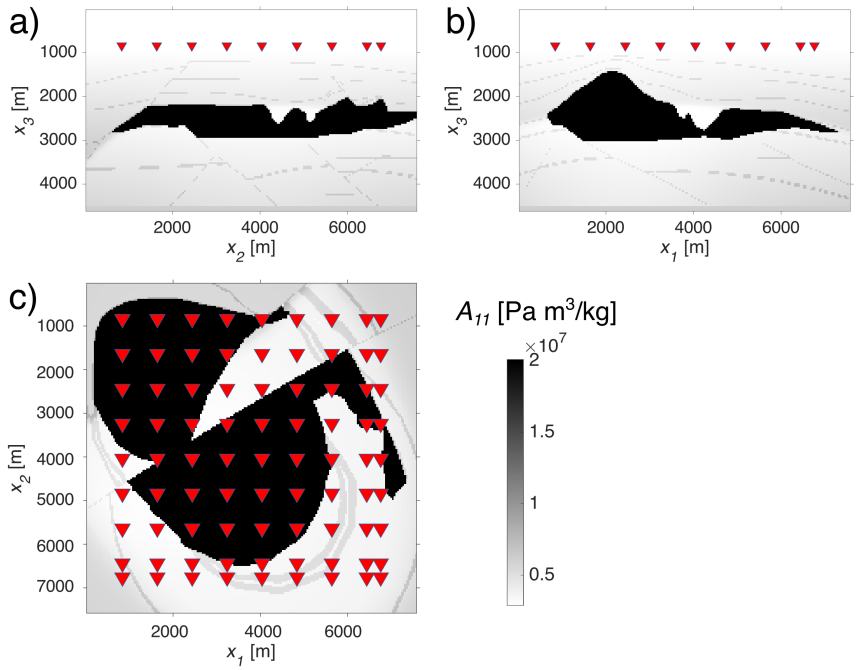

Figure 14: The modified 3D EAGE/SEG Salt model. We obtain our acoustic TTI model by $A_{11} = v^2$, $A_{33} = 1.4A_{11}$, $\eta = 0.2\frac{A_{11}}{max(A_{11})}$, $\alpha = \frac{\pi}{2}\frac{A_{11}}{max(A_{11})}$, $\beta = 2\pi\frac{A_{11}}{max(A_{11})}$, where v is the original velocity of 3D EAGE/SEG model. (a) Slice at $x_1 = 4400$ m. (b) Slice at $x_2 = 4400$ m. (c) Slice at $x_3 = 2800$ m. The down-pointing triangles are the imaging source locations projected on those planes. 216000 receivers are evenly distributed in this range, $x_1 \in [840, 12640]$ m, $x_2 \in [840, 12640]$ m, $x_3 = 840$ m.

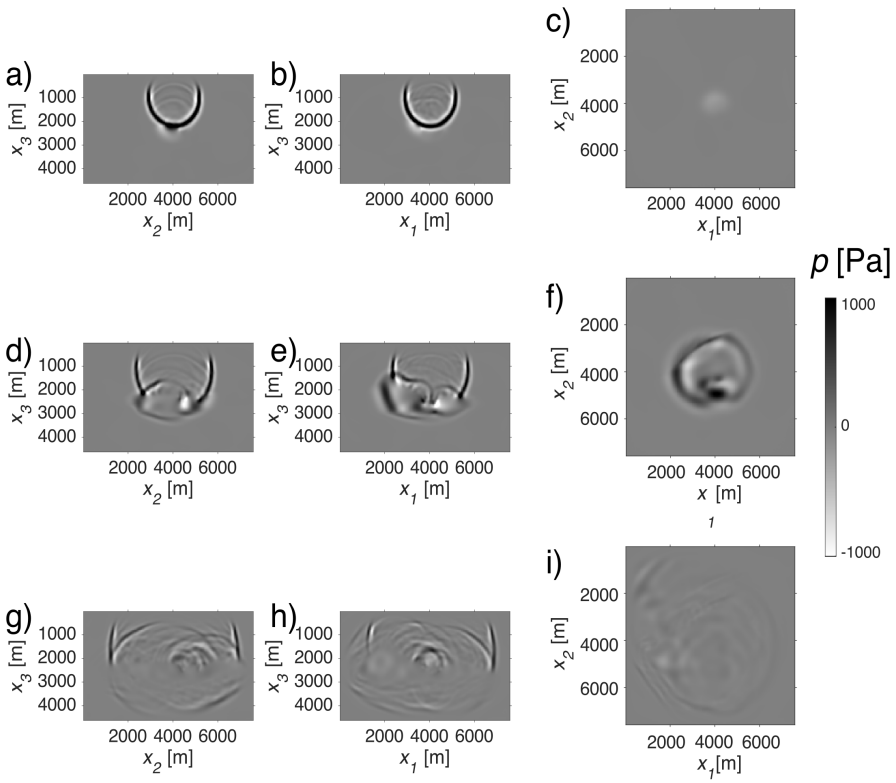

Figure 15: The solution of the wavefield by the proposed method. The source is placed at $[4440\ 4440\ 840]^T$ m. Source: Ricker wavelet, 7 Hz. The three rows are corresponding $t = 0.3,\ 0.4,\ 0.6$ s. The three columns are corresponding to the same slices with Figure 14 for (a), (b), and (c).

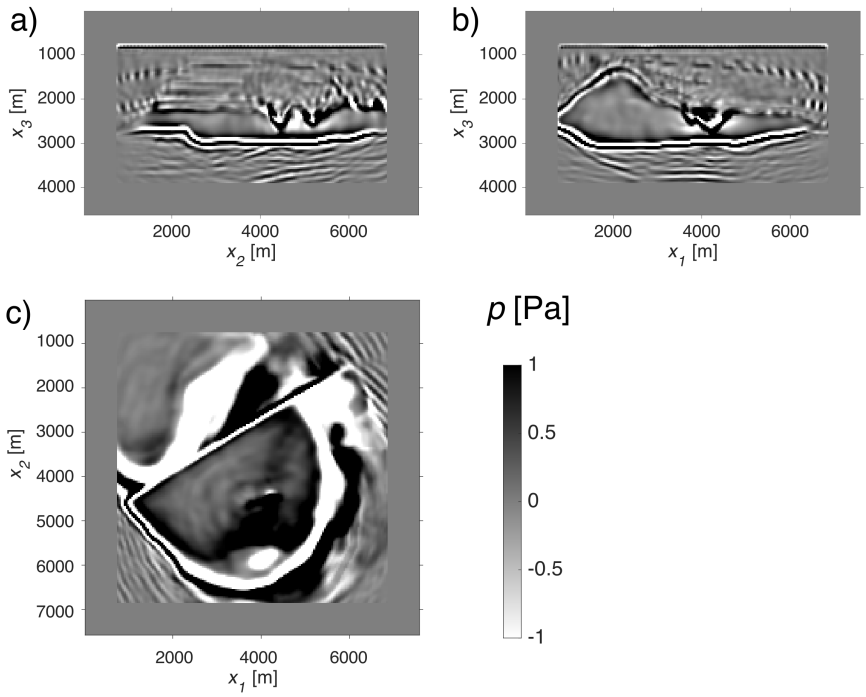

Figure 16: The RTM image for the model in Figure 14. Same slices with Figure 14 for (a), (b), and (c).